Diurnal and nocturnal cloud segmentation of ASI images using enhancement fully convolutional networks

Shi Chaojun[1], Zhou Yatong[1], Qiu Bo[1], He Jingfei[1], Ding Mu[1], Wei Shiya[1]

[1]School of Electronics and Information Engineering, Hebei University of Technology, Tianjin, 300401, China

Correspondence to: Zhou Yatong (zyt@hebut.edu.cn)

Abstract. Cloud segmentation plays a very important role in the astronomical observatory site selection. At present, few researchers segment cloud in the nocturnal All Sky Imager (ASI) images. This paper proposes a new automatic cloud segmentation algorithm which utilizes the advantages of deep learning fully convolutional networks (FCN) to segment cloud pixels from diurnal and nocturnal ASI images, named "enhancement fully convolutional networks" (EFCN). Firstly, all the ASI images in the data set from the Key Laboratory of Optical Astronomy at the National Astronomical Observatories of Chinese Academy of Sciences (CAS) are converted from the red-green-blue (RGB) color space to hue-saturation-intensity (HSI) color space. Secondly, the I channel of the HSI color space is enhanced by the histogram equalization. Thirdly, all the ASI images are converted from the HSI color space to RGB color space. Then after 100000 times iterative training based on the ASI images in the training set, the optimum associated parameters of the EFCN-8s model are obtained. Finally, we use the trained EFCN-8s to segment the cloud pixels of the ASI image in the test set. In the experiments our proposed EFCN-8s was compared with other four algorithms (OTSU, FCN-8s, EFCN-32s and EFCN-16s) using four evaluation metrics. Experiments show that the EFCN-8s is much more accurate in the cloud segmentation for diurnal and nocturnal ASI images than other four algorithms.

1 Introduction

Cloud plays an important role in the Earth's thermal balance and water cycle which is one of the important indicators for astronomical observatory site selection (Stephens, 2005). Cloud coverage and movements affect the time of astronomical observations. At present, cloud observations rely mainly on satellite remote sensing and ground-based observations. A detailed review has been given about the advantages and disadvantages on the satellite remote sensing and ground-based observations (Tapakis and Charalambides, 2013). Satellite cloud images can provide large scale distribution structure information of cloud in a wide range. Different types and distribution patterns of cloud can provide rich weather information, but the description accuracy of thin clouds and low cloud is not high enough to accurately reflect local range weather conditions and changes of the atmosphere. The ground-based cloud observation range is small, and it can provide local information such as cloud block size and arrangement. It has the advantages of flexible observation point, easy operation, convenient and fast, and generally mostly visible light image, with rich image information. However, if relying on the experience of observers to perform manual

observation, the observation result is easily restricted by human factors, resulting in the lack of objectivity and accuracy, and the automatic detection and recognition of the cloud images cannot be realized. Therefore, the development of automated cloud detection and identification equipments has become an inevitable trend.

With the development of hardware technologies such as charge-coupled device and digital image processing, many ground-based full-sky cloud measuring instruments have been successfully developed. Currently the most representative instruments include Whole Sky Imager(WSI; Johnson et al., 1989), Total Sky Imager(TSI; Long and Deluisi, 1998; Long et al., 2006), Infrared Cloud Imager(ICI; Shaw et al., 2005; Thurairajah and Shaw, 2005; Nugent et al., 2009; Nugent et al., 2013), All Sky Imager(ASI; Cazorla et al., 2008), Whole Sky Infrared Cloud Measuring System(WSIRCMS; Sun et al., 2008), Total Sky Cloud Imager(TCI; Yang et al., 2012), All-Sky Infrared Visible Analyzer(ASIVA; Klebe et al., 2014), Whole Sky Camera(WSC; Kuji et al., 2018), All Sky Camera (ASC; Aebi, 2018). The above instruments provide hardware support for analyzing ground-based cloud images, making automated observation of ground-based cloud images possible.

Benefiting from these cloud measuring instruments, many ground-based cloud segmentation algorithms have appeared. Atmospheric molecular scattering is inversely proportional to the fourth power of the wavelength, and cloud particle scattering is not closely related to wavelength, so the sky is blue and the cloud appears white in daytime. Therefore, the threshold algorithms become the mainstream for ground-based cloud detection. Long et al. (2006) proposed a cloud detection algorithm based on color thresholds to extract the regions of the cloud using 0.6 as a single fixed threshold in red-to-blue (R/B) ratio bands. Different from the ratio R/B, Heinle et al. (2010) revamped the criterion and adopted using the difference value of R-B to segment clouds. Then, the upper and lower thresholds for each attribute to segment the cloud were proposed, which are determined by the average and standard deviations of the saturation values (Souza-Echer et al., 2006). Yang et al. (2015) analyzed the imaging of color cameras and proposed a new algorithm, that is, green channel background subtraction adaptive threshold to automatically detect cloud within ground-based total-sky visible images. Yang et al. (2016) proposed an improved total sky cloud segmentation algorithm, clear sky background differencing (CSBD), using a real clear sky background to improve the cloud segmentation accuracy. To remove the difference of atmospheric scattering and obtain a homogeneous sky background, Yang et al. (2016) proposed a cloud segmentation algorithm using a new RGB channel operation by combining the advantages of the threshold and differencing algorithms.

Li et al. (2011) combined the fixed and adaptive threshold algorithm and proposed an effective cloud segmentation algorithm, named Hybrid Threshold Algorithm (HTA). Ghonima et al. (2012) compared the pixel red-blue ratio (RBR) to the RBR of a clear sky library (CSL) for more accurate cloud segmentation. Different from the various algorithms mentioned above, Calbo and Sabburg (2008) presented several features which are computed from the threshold image, extracted from statistical measurements of image texture, based on the Fourier transform of the image, and that can be useful for cloud segmentation of all-sky images. Peng et al. (2015) designed a classifier-based pipeline of identifying and tracking clouds in three-dimensional space to utilize all three total sky imagers for multi-source image correction to enhance the overall accuracy of cloud detection. Shi et al. (2017) used a superpixels based graph model (GM) to integrate multiple source information, and proposed a new ground-based cloud detection algorithm to solve the problem that a single information source is difficult to split the cloud from

the clear sky. By analyzing components and different color spaces using partial least squares regression, Dev et al. proposed a supervised segmentation framework to segment ground-based cloud pixels without any manually defined parameters (Dev et al., 2017). Neto et al. (2010) described a new segmentation algorithm using Bayesian inference and multidimensional Euclidean geometric distance to segment the cloud and sky patterns in image pixels on the RGB color space. Calbo et al. (2017) proposed the sensitivity as the thin boundary between clouds and aerosols. Roman et al. (2017) presented a new cloud segmentation strategy using high dynamic range images from a sky camera and ceilometer measurements, which is also able to segment the obstruction of the sun. With the development of neural networks, algorithms in the field of deep learning (LeCun et al., 1989; Ning et al., 2005; Hinton and Salakhutdinov, 2006; Krizhevsky et al., 2017; Shelhamer et al., 2017) began to be applied to cloud segmentation. Moreover, Cheng and Lin (2017) segmented cloud using supervised learning with multi-resolution features. The features include multi-resolution information and local structure extracted from local image patches with different sizes.

The algorithms proposed above are all for segmenting cloud from total-sky images in the daytime. For nocturnal ASI images cloud and sky background, pixel values are very low and difficult to distinguish. The effect of sunlight on nocturnal ASI images is very weak, but weak light such as moonlight and starlight have a great influence on it. Therefore nocturnal ASI images are more noisy than diurnal ASI images. Gacal et al. (2016) proposed a algorithm to segment nocturnal cloud images using a single fixed threshold method. The algorithm used temporal averaging to estimate the cloud cover based on the segmentation results of the images near the zenith. However, due to factors such as moonlight, lighting, and weather conditions, it is difficult to accurately segment cloud pixels by a single fixed threshold method. Dev et al. (2017) proposed a superpixel-based algorithm to segment nocturnal sky/cloud images, and the first nocturnal sky/cloud image segmentation database was released to the public in this paper. Dev et al. (2019) first integrated diurnal and nocturnal images segmentation into one framework. They proposed a light-wight deep-learning architecture named CloudSegNet to segment them and achieved good results. However, so far, few researchers have segmented the nocturnal cloud images. Accordingly, we propose a new automatic cloud segmentation algorithm which utilizes the advantages of deep learning algorithm fully convolutional networks (FCN), named “enhancement fully convolutional networks” (EFCN). Section 2 describes the device ASI and the data set ASI images. Section 3 shows the proposed EFCN in detail. In Sect. 4, we conducted three sets of experiments to segment cloud pixels by the proposed algorithm and other four algorithms. Then we analyzed the experimental results in detail based on four evaluation metrics. Finally, Sect. 5 gives a summary and some suggestions in the next work.

2 Device and data description

The cloud images used in this paper are taken by ASI, which are provided by the Key Laboratory of Optical Astronomy at the National Astronomical Observatories of CAS. Figure 1(a) demonstrates the device of ASI. Like other all-sky cloud measuring instruments, the key equipment of the ASI are composed of a fisheye lens, an industrial camera, and a clear glass cover. The device can cover a field of view larger than 180º. The camera protected by the clear glass cover to prevent the wind, rain, snow

and fog, can capture one 24-bit RGB color space ASI image per 3s. The resolution of the original RGB color space ASI images is 2592×1728 pixels as shown in Fig. 1(b). We randomly select 1124 original RGB color space ASI images to construct our data set, including 369 original diurnal ASI images and 755 original nocturnal ASI images. We define the original ASI images taken during 7:00 in the morning until 7:00 at night as diurnal ASI images and taken during 7:00 at night until 7:00 in the next morning as nocturnal ASI images. In the data set, we randomly select 1054 original RGB color space ASI images as the training set, including 343 original diurnal ASI images and 711 original nocturnal ASI images. Another 70 original ASI images in the data set are selected as the test set, with 26 original diurnal ASI images and 44 original nocturnal ASI images.

The effective area of the original RGB color space ASI images is a circular region whose diameter includes 1408 pixels. Therefore, each image of the data set is resized into 1408×1408 pixels as shown in Fig. 1(c). We manually label the pixels belonging to cloud of each resized ASI image in the training set and test set using the software LabelMe, creating the ground truth of the data set. We first open the image to be labeled in the software LabelMe. Second, we label the cloud pixels with multiple closed curves to ensure the cloud pixels inside the curve and sky background outside the curve. And then, we set the labeled cloud pixel to blue and the unlabeled sky background to black. A json file is generated after label. Finally, we convert the json file into a labeled image. Figure 2 shows eight diurnal and nocturnal resized RGB color space ASI images in the data set and the corresponding ground truth of the eight diurnal and nocturnal resized ASI images. Figure 2(a) is the diurnal resized ASI images in the data set, and their corresponding ground truth are shown in Fig. 2(b). Figure 2(c) denotes the nocturnal resized ASI images in the data set. Figure 2(d) represents the corresponding ground truth of the nocturnal resized ASI images from Fig. 2(c). In Fig. 2(b) and Fig. 2(c), white pixels indicates the cloud and black pixels indicates the sky background. The device used for training is a server equipped with a NVIDIA GeForce GTX 1080ti×2 with 11×2 of memory. The deep learning framework used in the experiments is TensorFlow, and the software programming environment is Python3.5.

3 Automatic cloud segmentation algorithm

This section describes the proposed EFCN which utilizes the deep learning algorithm FCN to segment cloud pixels from diurnal and nocturnal ASI images. Firstly, we sketch the proposed EFCN, and then the details of EFCN are described.

3.1 Sketch on EFCN for ASI images segmentation

The proposed EFCN is an improvement of FCN. Firstly, the resized ASI images in the data set are converted from the RGB color space to the HSI color space (RGB-HSI). Secondly, the I channel is separated from HSI color space. And then the I channel is equalized by the histogram equalization, in order to enhance the intensity and remain constant the saturation and hue of the resized ASI images. Thirdly, the ASI images in the data set are converted from the HSI color space back to the RGB color space (HSI-RGB), and use the training set to train EFCN model. The associated parameters are obtained. Finally, the test set is input the trained model to segment cloud pixels in the ASI images for detecting the performance of the model. The different steps will be explained in the following subsections respectively.

3.2 EFCN

Fully convolutional networks are a powerful visual deep learning algorithm for semantic segmentation (Shelhamer et al., 2017). Replacing the fully connected layers of the traditional convolutional neural networks (CNN) with the convolutional layers, the FCN reduces the network parameters, improves the segmentation speed and shows a good result on semantic segmentation through trained end-to-end, and pixels-to-pixels (Cheng and Lin, 2017). The basic components of FCN include convolutional layers, pooling layers, activation functions and deconvolutional layers, as shown in Fig. 3. At present, FCN have been widely used in medical images processing, remote sensing images processing, computer vision and other fields (Yuan et al., 2017; Jiao et al., 2017; Lopez-Linares et al., 2018; Zeng and Zhu, 2018).

However, the FCN has some disadvantages to segment cloud pixels in diurnal and nocturnal ASI images. Therefore, the EFCN is proposed based on the VGG-16 network, to replace the fully connected layer of VGG-16 with a convolutional layer and outputs an upsampled prediction. Enhancement fully convolutional networks can accept input diurnal and nocturnal ASI images in any size, producing a prediction for each pixel, the output the prediction being the same size as the input ASI image. Unlike CNN, the EFCN can classify ASI images at the pixel level. Figure 4 illustrates the detailed architecture of EFCN model including RGB-HSI layer, histogram equalization layer, HSI-RGB layer, convolutional layers, pooling layers, deconvolutional layers, skip architecture~~,~~ and activation functions.

Images of All Sky Imager are usually not very clear due to the complex weather conditions, especially at night. We need to use image enhancement method to process the ASI images for better features and visual effects. Using the histogram equalization to equalize any channel of the RGB color space cause a change in the hue and saturation of ASI images. However, the ASI images are enhanced in the I channel of HSI color space, and the hue and saturation channels remain constant. We convert the ASI images from the RGB to HSI color space, and use the histogram equalization to equalize the I channel of the HSI color space. Then the images are converted from the HSI back to RGB color space to obtain the enhanced images. This method is stable and fast. The EFCN model in Fig. 4 has eight convolutional layers. The number of convolution kernels is different for each convolutional layer. We define the size and stride of convolutional kernel. Each convolutional kernel has the same size and stride. The size is 3×3 and the stride is 1. The role of the convolutional layer is to extract features from images, and different convolutional layers can extract different features. In order to ensure that the size of the feature map after convolution is consistent with the size before convolution, we use zero pad operation. The convolution calculation formula can be expressed as follows:

$$x^{(l)} = \sum_{u \in N_v} a_u^{(l-1)} n_{uv}^{(l)} + b_C^{(l)}$$
$$a_u^{(l)} = f(x_v^{(l)}) \quad (1)$$

where l represents the number of layers in the neural network, v represents feature maps, n represents convolutional kernels, b_C represents the bias of output feature maps, N_v represents the collection of input feature maps, and f represents activation

function. This paper adopts the Rectified Linear Unit (ReLU) as activation function. The ReLU activation function is defined as follows:

$$f(x_v^{(l)}) = \max(0, x_v^{(l)}) \tag{2}$$

where l represents the number of layers in the neural network, v represents feature maps. Pooling operation is a down-sampling process. The pooling layer is located after the convolution layer, which can further extract features, reduce the size of the feature maps, speed up calculations, and prevent overfitting. This paper uses the max-pooling method. Through the max-pooling operation, the size of the feature maps is reduced by half. After eight times of convolution operation and five times of pooling operation as shown in Fig. 4, the resolution of the input ASI image is reduced by two, four, eight, sixteen, thirty-two times. Meanwhile we get two heatmaps as shown in map6 of Fig. 4. Heatmaps are one of the most important high-dimensional feature maps. Our goal is to separate the cloud from the sky background, so we need to get two heatmaps. Following that, a very important step is to upsample the heatmaps so that the two heatmaps in map6 are enlarged to the same size of the input ASI image.

We use deconvolution operation to upsample the two heatmaps in map6 that output from the last convolutional layer, enlarge them by 32 times and return them to the same size as the input ASI image, while retaining the spatial information in the original input image, so that we can generate and predict each pixel. Finally, we use the argmax1 function to classify each pixel. The pixels classification is determined by the maximum value of the corresponding pixels positions of the two heatmaps in map7. We get the 32 upsample prediction and refer this model as EFCN-32s. However, EFCN-32s is too rough to restore the features in the input image well. The segmentation result is not very accurate and some details cannot be restored. Therefore, we propose a skip connection structure. The heatmaps in map6 are upsampled by a factor of 2 through the deconv2 layer and then integrates with the feature maps in map4. The integrated feature maps are upsampled by a factor of 16 through the deconv3 layer to obtain the feature maps of the same size as the input ASI image. We get the 16 upsample prediction after the argmax2 function and refer this model as EFCN-16s. The integrated feature maps are upsampled by a factor of 2 through the deconv4 layer and then integrated with the feature maps in map3. The second integrated feature maps are upsampled by a factor of 8 through the deconv5 layer to obtain the feature maps of the same size as the input ASI image. We get the 8 upsample prediction after the argmax3 function and refer this model as EFCN-8s.

Table 1 summarize the parameters of the proposed EFCN which have been shown in Fig. 4. Here ‘HE’ represents histogram equalization, ‘conv’ represents the convolution operation, ‘pool’ represents max-pooling operation, and ‘deconv’ represents deconvolution operation. The upsampled prediction is as the same size as the input ASI image.

As a summary, the complete proposed automatic cloud segmentation based on EFCN-8s is summarized in the following Algorithm 1.

Algorithm 1 EFCN-8s

Input: diurnal and nocturnal ASI images and the corresponding ground truth of training set and test set.

1: Convert all the ASI images of training set and test set from the RGB to HSI color space;

2: Use the histogram equalization method to equalize the I channel of the HSI color space;

3: Convert all the ASI images of training set and test set from the HSI to RGB color space;

4: Use the training set including ASI images and the corresponding ground truth as the input of the EFCN-8s model, train the model, perform 100,000 iterations, and save the optimum associated parameters;

5: Utilize the trained EFCN-8s model to segment the cloud pixels in the ASI images of test set;

6: Output the segmented result.

We illustrate the framework of the proposed automatic cloud segmentation algorithm based on EFCN-8s in Fig. 5. Figure 5(a) represents the input test ASI image of the EFCN-8s model captured in daytime which is enhanced by the method of histogram equalization as shown in Fig. 5(b). Figure 5(c) represents the cloud segmentation result using the trained EFCN-8s model. Figure 5(d) represents the input test ASI image of the EFCN-8s model captured in night which is enhanced by the method of histogram equalization as shown in Fig. 5(e). Figure 5(f) represents the cloud segmentation result using the trained EFCN-8s model.

4 Experiments results

We design three sets of experiments to segment the cloud pixels from the resized diurnal and nocturnal ASI images, and analyze the experimental results in detail based on four evaluation metrics.

4.1 Experiments

We randomly select 1124 ASI images as our data set, including 369 diurnal ASI images and 755 nocturnal ASI images. We use the software LabelMe to label these ASI images. The 1054 ASI images and the corresponding labels are randomly selected as the training set, including 343 diurnal image~~,~~ and 711 nocturnal images. Another 70 ASI images and corresponding labels are used as test set, including 26 diurnal ASI images~~,~~ and 44 nocturnal ASI images. The training set is iteratively trained on the EFCN-8s model, which is iterated 100000 times, and the best model parameters are obtained. The data from the test set are used to verify the robustness and accuracy of EFCN-8s. We design three sets of experiments to segment cloud pixels from the ASI images. In the first set of experiments, the cloud pixels are segmented in the diurnal ASI images. In the second set of experiments, the cloud pixels are segmented in the nocturnal ASI images. In the third set of experiments, the cloud pixels are segmented in the diurnal and nocturnal ASI images.

In the first set of experiments, we used the proposed EFCN-8s, EFCN-16s, EFCN-32s, FCN-8s, and OTSU algorithms to segment cloud pixels in the diurnal ASI images respectively. OTSU algorithm is a classic automatic threshold selection algorithm for images segmentation without parameter and supervision (Otsu, 1979). This algorithm is one of the most commonly used image segmentation algorithms by discriminant criterion to determine the optimal threshold without any prior information. The cloud segmentation results are shown in Fig. 6. Figure 6(a) represents the resized diurnal ASI images, and

Fig. 6(b) shows the enhanced diurnal ASI images. Figure 6(c) denotes the ground truth of the corresponding ASI images. The results of cloud segmentation by OTSU, FCN-8s, EFCN-32s, EFCN-16s, EFCN-8s are shown in Fig. 6(d)-(h) respectively.

As shown in the Fig. 6, the OTSU has good cloud segmentation accuracy under the clear sky background without sunlight. However, the segmentation accuracy is poor when the sunlight is visible in the images or the brightness of the images is low. For the EFCN-32s, the recognition accuracy is improved compared with the OTSU algorithm. The EFCN-16s segments cloud better than EFCN-32s, but the details of cloud are not recognized. In addition to the diurnal ASI images with visible sun, the segmentation performance of the FCN-8s is usually good. The recognition accuracy of the EFCN-8s is very good for almost all the diurnal ASI images. The details of the cloud can be identified without the influence of sunlight.

In the second set of experiments, we used the proposed EFCN-8s to segment cloud pixels in the nocturnal ASI images and compared the result with the EFCN-16s, EFCN-32s, FCN-8s and OTSU algorithms. The different experimental segmentation results are shown in Fig. 7. Figure 7(a) represents the resized nocturnal ASI images, and Fig. 7(b) shows the enhanced nocturnal ASI images. Figure 7(c) denotes the ground truth of the corresponding ASI images. The different results of cloud segmentation are shown in Fig. 7(d)-(h) respectively.

As shown in Fig. 7, the proposed EFCN-8s shows the best segmentation results. The results of EFCN-32s, EFCN-16s and FCN-8s are better, and the segmentation results are close. However, the details of cloud are not recognized. The experimental results using OTSU are very poor. Most of the sky background pixels are mistakenly segmented into cloud pixels.

In the third set of experiments, the cloud pixels in the diurnal and nocturnal ASI images are segmented simultaneously. The segmentation results of the proposed EFCN-8s and other four algorithms are shown in Fig. 8. Figure 8(a) represents the diurnal ASI image, the ground truth of the corresponding ASI image and the segmentation results of the proposed EFCN-8s and other four algorithms. Figure 8(b) represents the nocturnal ASI image, the ground truth of the corresponding ASI image and the segmentation results of the proposed EFCN-8s and other four algorithms. As shown in Fig. 8, consistent with the results obtained in experiment 1 and experiment 2, the proposed EFCN-8s has the best segmentation results, which verifies that the proposed algorithm is robust.

4.2 Evaluation metrics

In order to better evaluate the results of the experiments, we adopt four effective evaluation metrics to analyze the experimental results which covered pixel accuracy and region intersection over union (IU) (Shelhamer et al., 2017). The four effective evaluation metrics including pixel accuracy (pixel acc), mean accuracy (mean acc), mean IU and frequency weighted IU (fw IU) are defined as follows:

$$\text{pixel acc} = \frac{\sum_{i=1}^{k} p_{ii}}{\sum_{i=1}^{k}\sum_{j=1}^{k} p_{ij}} \tag{3}$$

$$\text{mean acc} = \frac{1}{k}\sum_{i=1}^{k}\frac{p_{ii}}{\sum_{j=1}^{k} p_{ij}} \tag{4}$$

$$\text{mean IU} = \frac{1}{k}\sum_{i=1}^{k}\frac{p_{ii}}{\sum_{j=1}^{k}p_{ij}+\sum_{j=1}^{k}p_{ji}-p_{ii}} \tag{5}$$

$$\text{fw IU} = \frac{1}{\sum_{i=1}^{k}\sum_{j=1}^{k}p_{ij}}\sum_{i=1}^{k}\frac{p_{ii}}{\sum_{j=1}^{k}p_{ij}+\sum_{j=1}^{k}p_{ji}-p_{ii}} \tag{6}$$

where pixel accuracy (pixel acc), mean accuracy (mean acc), frequency weighted IU (fw IU), mean IU, k means that each ASI image in the test set can be segmented into k class, including clouds and sky background; p_{ij} represents the number of pixels of class i predicted to class j. Among the above four metrics, mean IU is the most commonly used metric because it is simple and representative.

4.3 Experiments results comparison

To better demonstrate the performance of the proposed EFCN-8s, we adopt four evaluation metrics defined in the previous section to compare the segmentation results with other algorithms including OTSU, FCN-8s, EFCN-32s and EFCN-16s algorithms.

Table 2 lists the performance of different algorithms on the cloud segmentation of diurnal ASI images in the first set of experiments. From Tables 2, we have the following observations. Firstly, the mean IU in the traditional OTSU result is 0.6235. The mean IU of the deep learning algorithm FCN-8s is raised by 0.1565 to 0.7800. The EFCN-32s based on VGG-16 increased the mean IU by 0.8048. The EFCN-16s add the skip connection structure that integrate the features of map6 and map5, resulting in a mean IU of 0.8049. The proposed EFCN-8s integrate the features of map 6, map 5 and map 4, achieving a significant improvement to 0.8481 mean IU. Secondly, skip connection structure and image enhancement can improve the accuracy of segmentation. Moreover, we can find the proposed algorithm works better for diurnal ASI images segmentation.

Table 3 lists the performance of different algorithms on the cloud segmentation of nocturnal ASI images in the second set of experiments. For nocturnal ASI images, the proposed EFCN-8s demonstrates strong advantages. When compared with other algorithms, it shows an increase of 0.1673 in pixel acc compared with OTSU, an increase of 0.0206 in mean acc compared with FCN-8s, an increase of 0.0433 in mean IU compared with EFCN-32s~~,~~ and an increase of 0.0158 in fw IU compared with EFCN-16s.

Compared Table 2 and Table 3, we can get the following observations. Firstly, the traditional threshold algorithm OTSU has a better segmentation result on diurnal ASI images than nocturnal ASI images. Secondly, the deep learning algorithms include FCN-8s, EFCN-32s, EFCN-16s~~,~~ and EFCN-8s, can extract the deep features of the ASI images and integrate multiple features. At the same time, due to the influence of sunlight, the nocturnal ASI images segmentation results are better than the diurnal ASI images.

Table 4 lists the performance of different algorithms on the cloud segmentation of diurnal and nocturnal ASI images in the third set of experiments. Table 4 shows that the results obtained in the third set of experiments are consistent with the first and second set of experiments. The proposed EFCN-8s has the best segmentation results compared with the other four algorithms

(OTSU, FCN-8s, EFCN-32s and EFCN-16s). The mean IU of the proposed EFCN-8s in experiment 3 increases by 0.0205 compared with experiment 1 and decreases by 0.0163 compared with experiment 2. This result verifies that the proposed EFCN-8s is robust.

5 Conclusions

The cloud segmentation is a huge challenge for astronomical researchers today. This paper proposed a new automatic cloud segmentation algorithm EFCN-8s to segment cloud pixels from diurnal and nocturnal ASI images. The cloud images were taken by ASI provided by the Key Laboratory of Optical Astronomy at the National Astronomical Observatories of CAS. We used the software LabelMe to semantically label the ASI images and created the ground truth. The proposed EFCN-8s was based on VGG-16 net. Histogram equalization enhances the intensity of the images, and the skip connection integrated the different features of the image together. The two operations including histogram equalization and the skip connection were applied to increase the segmentation performance.

To verify the performance of the proposed algorithm, we designed three sets of experiments. In the first set of experiments, the proposed EFCN-8s was used to segment the diurnal ASI images. It could reduce the influence of the sun and a good segmentation result was obtained on the test set. In the second set of experiments, the EFCN-8s could extract multidimensional features for nighttime ASI images and also had good segmentation results. In the third set of experiments, the cloud pixels in the diurnal and nocturnal ASI images were segmented simultaneously. The results were consistent with the first and second set of experiments which verified that the proposed EFCN-8s was robust. After that, the EFCN-8s was compared with other four algorithms including OUSU, FCN-8s, EFCN-32s and EFCN-16s. To better verify the performance, we adopted four evaluation metrics to measure the segmentation results. The results show that the EFCN-8s is much more accurate at cloud segmentation for diurnal and nocturnal ASI images than other four algorithms.

It should be noted that the EFCN-8s still has some limitations. Firstly, it can be seen from Table 1 and 2 that the EFCN-8s is better than diurnal ASI images for nocturnal ASI images segmentation. This may be due to interference from the sun. Secondly, since the ground truth of the data set is manually labeled by us, it has some errors for the true values of cloud. In the next work, we will remove the interference of the sun at first, and use a more advanced approach to label the data sets.

References

Aebi, C., Grobner, J., and Kampfer, N.: Cloud fraction determined by thermal infrared and visible all-sky cameras, Atmos. Meas. Tech., 11, 5549-5563, https://doi.org/10.5194/amt-11-5549-2018, 2018.

Calbo, J. and Sabburg, J.: Feature extraction from whole-sky ground-based images for cloud-type recognition, J. Atmos. Ocean. Tech., 25, 3-14, https://doi.org/10.1175/2007JTECHA959.1, 2008.

Calbo, J., Long, C. N., Gonzalez, J. A., Augustine, J., and McComiskey, A.: The thin border between cloud and aerosol: Sensitivity of several ground based observation techniques, Atmos. Res., 196, 248-260, https://doi.org/10.1016/j.atmosres.2017.06.010, 2017.

Cazorla, A., Olmo, F. J., and Alados-Arboledasl, L.: Development of a sky imager for cloud cover assessment, J. Opt. Soc. Am. A., 25, 29-39, https://doi.org/10.1364/JOSAA.25.000029, 2008.

Cheng, H. Y. and Lin, C. L.: Cloud detection in all-sky images via multi-scale neighborhood features and multiple supervised learning techniques, Atmos. Meas. Tech., 10, 199-208, https://doi.org/10.5194/amt-10-199-2017, 2017.

Dev, S., Lee, Y. H., and Winkler, S.: Color-based segmentation of sky/cloud images from ground-based cameras, IEEE J. Sel. Top. Appl., 10, 231-242, https://doi.org/10.1109/JSTARS.2016.2558474, 2017.

Dev, S., Nautiyal, A., Lee, Y. H., and Winkler, S.: CloudSegNet: A Deep Network for Nychthemeron Cloud Image Segmentation, IEEE Geosci. Remote S., 2019.

Dev, S., Savoy, F. M., Lee, Y. H., and Winkler, S.: Nighttime sky/cloud image segmentation, 2017 IEEE International Conference on Image Processing, https://doi.org/10.1109/ICIP.2017.8296300, 2017.

Gacal, G. F. B., Antioquia, C., and Lagrosas, N.: Ground-based detection of nighttime clouds above Manila Observatory (14.64 degrees N, 121.07 degrees E) using a digital camera, Appl. Optics, 55, 6040-6045, https://doi.org/10.1364-/AO.55.006040, 2016.

Ghonima, M. S., Urquhart, B., Chow, C. W., Shields, J. E., Cazorla, A., and Kleissl, J.: A method for cloud detection and opacity classification based on ground based sky imagery, Atmos. Meas. Tech., 5, 2881–2892, https://doi.org/10.5194/amt-5-2881-2012, 2012.

Heinle, A., Macke, A., and Srivastav, A.: Automatic cloud classification of whole sky images, Atmos. Meas. Tech., 3, 557-567, https://doi.org/10.5194/amt-3-557-2010, 2010.

Hinton, G. E. and Salakhutdinov, R. R.: Reducing the dimensionality of data with neural networks, Science, 313, 504-507, https://doi.org/10.1126/science.1127647, 2006.

Jiao, L. C., Liang, M. M., Chen, H., Yang, S., Y., Liu, H. Y., and Cao, X. H.: Deep fully convolutional network-based spatial distribution prediction for hyperspectral image classification, IEEE T. Geosci. Remote, 55, 5585-5599, https://doi.org/10.1109/TGRS.2017.2710079, 2017.

Johnson, R.W., Hering, W. S., and Shields, J. E.: Automated visibility and cloud cover measurements with a solid-state imaging system, University of California, San Diego, Scripps Institution of Oceanography, Marine Physical Laboratory, SIO89-7, GL-TR-89-0061, 1989.

Klebe, D. I., Blatherwick, R. D., and Morris, V. R.: Ground-based all-sky mid-infrared and visible imagery for purposes of characterizing cloud properties, Atmos. Meas. Tech., 7, 637–645, https://doi.org/10.5194/amt-7-637-2014, 2014.

Krizhevsky, A., Sutskever, I., and Hinton, G. E.: Imagenet classification with deep convolutional neural networks, Commun. Acm., 60, 84-90, https://doi.org/10.1145/3065386, 2017.

Kuji, M., Murasaki, A., Hori, M., and Shiobara, M.: Cloud fractions estimated from shipboard whole-sky camera and ceilometer observations between east Asia and Antarctica, J. Meteorol. Soc. Jpn., 96, 201-214, https://doi.org/10.2151/jmsj.2018-025, 2018.

LeCun, Y., Boser, B., Denker, J. S., Henderson, D., Howard, R. E., Hubbard, W., and Jackel, L. D.: Backpropagation applied to handwritten zip code recognition, Neural Comput., 11, 541-551, https://doi.org/10.1162/neco.1989.1.4.541,1989.

Li, Q. Y., Lu, W. T., and Yang, J.: A hybrid thresholding algorithm for cloud detection on ground-based color images, J. Atmos. Ocean. Tech., 28, 1286-1296, https://doi.org/10.1175/JTECH-D-11-00009.1, 2011.

Long, C. N. and Deluisi, J. J.: Development of an automated hemispheric sky imager for cloud fraction retrievals, in: Proc. 10th Symp. on meteorological observations and instrumentation, 11-16 January 1998, Phoenix, Arizona, USA 171-174,1998.

Long, C. N., Sabburg, J. M., Calbo, J., and Pages, D.: Retrieving cloud characteristics from ground-based daytime color all-sky images, J. Atmos. Ocean. Tech., 23, 633-652, https://doi.org/ 10.1175/JTECH1875.1, 2006.

Lopez-Linares, K., Aranjuelo, N., Kabongo, L., Maclair, G., Lete, N., Ceresa, M., Garcia-Familiar, A., Macia, I., and Ballester, M. A. G.: Fully automatic detection and segmentation of abdominal aortic thrombus in post-operative CTA images using deep convolutional neural networks, Med. Image Anal., 46, 203-214, https://doi.org/10.1016/j.media.2018.03.010, 2018.

Neto, S. L. M., von Wangenheim, A., Pereira, E. B., and Comunello, E.: The use of euclidean geometric distance on rgb color space for the classification of sky and cloud patterns, J. Atmos. Ocean. Tech., 27, 1504-1517, https://doi.org/10.1175/2010JTECHA1353.1, 2010.

Ning, F., Delhomme, D., LeCun, Y., Piano, F., Bottou, L., and Barbano, P. E., Toward automatic phenotyping of developing embryos from videos, IEEE T. Image Process., 14, 1360-1371, https://doi.org/10.1109/TIP.2005.852470, 2005.

Nugent, P. W., Shaw, J. A., and Piazzolla, S.: Infrared cloud imaging in support of Earth-space optical communication, Opt. Express, 17, 7862-7872, https://doi.org/ 10.1364/OE.17.007862, 2009.

Nugent, P. W., Shaw, J. A., and Pust, N. J.: Correcting for focal-plane-array temperature dependence in microbolometer infrared cameras lacking thermal stabilization, Opt. Eng., 52, https://doi.org/ 10.1117/1.OE.52.6.061304, 2013.

Otsu, N.: A Threshold Selection Method from Gray-Level Histograms, IEEE T. Syst. Man Cyb., 9, 62-66, https://doi.org/10.1109/TSMC.1979.4310076, 1979.

Peng, Z. Z., Yu, D. T., Huang, D., Heiser, J., Yoo, S., and Kalb, P.: 3D cloud detection and tracking system for solar forecast using multiple sky imagers, Sol. Energy, 118, 496-519, https://doi.org/10.1016/j.solener.2015.05.037, 2015.

Roman, R., Cazorla, A., Toledano, C., Olmo, F. J., Cachorro, V. E., de Frutos, A., and Alados-Arboledas, L.: Cloud cover detection combining high dynamic range sky images and ceilometer measurements, Atmos. Res., 196, 224-236, https://doi.org/10.1016/j.atmosres.2017.06.006, 2017.

Shaw, J. A., Nugent, P. W., Pust, N. J., Thurairajah, b., and Mizutani, K.: Radiometric cloud imaging with an uncooled microbolometer thermal infrared camera, Opt. Express, 13, 5807-5817, https://doi.org/10.1364/OPEX.13.005807, 2005.

Shelhamer, E., Long, J., and Darrell, T.: Fully convolutional networks for semantic segmentation, IEEE T. Pattern. Anal., 39, 640-651, https://doi.org/10.1109/TPAMI.2016.2572683, 2017.

Shi, C. Z., Wang, Y., Wang, C. H., and Xiao, B. H.: Ground-based cloud detection using graph model built upon superpixels, IEEE Geosci. Remote S., 14, 719-723, https://doi.org/ 10.1109/LGRS.2017.2676007, 2017.

Souza-Echer, M. P., Pereir-A, E. B., Bins, L. S., and Andrade, M.A.R.: A simple method for the assessment of the cloud cover state in high-latitude regions by a ground-based digital camera, J. Atmos. Ocean. Tech., 23, 437-447, https://doi.org/10.1175/JTECH1833.1, 2006.

Stephens, G. L.: Cloud feedbacks in the climate system: a critical review, J. Climate, 18, 237-273, https://doi.org/10.1175/JCLI-3243.1, 2005.

Sun, X. J., Gao, T. C., Zhai, D. L., Zhao, S. J., and Lian, J. G.: Whole sky infrared cloud measuring system based on the uncooled infrared focal plane array, Infrared and Laser Engineering, 37, 761-764, 2008.

Tapakis, R. and Charalambides, A. G.: Equipment and methodologies for cloud detection and classification: a review, Sol. Energy, 95, 392-430, https://doi.org/10.1016/j.solener.2012.11.015, 2013.

Thurairajah, B. and Shaw, J. A.: Cloud statistics measured with the infrared cloud imager (ICI), IEEE T. Geosci. Remote, 43, 2000-2007, https://doi.org/ 10.1109/TGRS.2005.853716, 2005.

Yang, J., Lu, W., Ma, Y., and Yao, W.: An automated cirrus cloud detection method for a ground-based cloud image, J. Atmos. Ocean. Tech., 29, 527–537, https://doi.org/10.1175/JTECH-D-11-00002.1, 2012.

Yang, J., Min, Q., Lu, W., Yao, W., Ma, Y., Du, J., Lu, T., and Liu, G.: An automated cloud detection method based on the green channel of total-sky visible images, Atmos. Meas. Tech., 8, 4671–4679, https://doi.org/10.5194/amt-8-4671-2015, 2015.

Yang, J., Min, Q. L., Lu, W. T., Ma, Y., Yao, W., Lu, T. S., Du, J., and Liu, G. Y.: A total sky cloud detection method using real clear sky background, Atmos. Meas. Tech., 9, 587–597, https://doi.org/10.5194/amt-9-587-2016, 2016.

Yang, J., Min, Q. L., Lu, W. T., Ma, Y., Yao, W., and Lu, T. S.: An RGB channel operation for removal of the difference of atmospheric scattering and its application on total sky cloud detection, Atmos. Meas. Tech.,10, 1191-1201, https://doi.org/10.5194/amt-10-1191-2017, 2017.

Yuan, Y. D., Chao, M., and Lo, Y. C.: Automatic skin lesion segmentation using deep fully convolutional networks with Jaccard distance, IEEE T. Med. Imaging, 36, 1876-1886, https://doi.org/10.1109/TMI.2017.2695227, 2017.

Zeng, D. D. and Zhu, M.: Background subtraction using multiscale fully convolutional network, IEEE Access, 6, 16010-16021, https://doi.org/ 10.1109/ACCESS.2018.2817129, 2018.

(a) **(b)** **(c)**

Figure 1: Device of ASI and ASI image. (a) device of ASI including a fisheye lens, an industrial camera and a clear glass cover, (b) original RGB color ASI image (2592×1728 pixels), (c) resized RGB color ASI image of (b) (1408×1408 pixels).

(a)

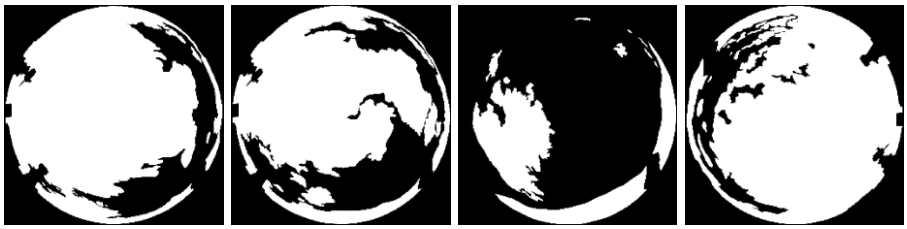

(b)

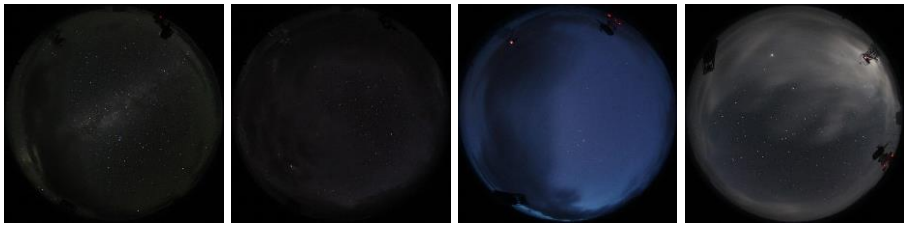

(c)

(d)

Figure 2. Diurnal and nocturnal original RGB color ASI images in the data set and the corresponding ground truth of the ASI images. (a) diurnal original RGB color ASI images in the data set, (b) corresponding ground truth ASI images from (a), (c) nocturnal original RGB color ASI images in the data set, (d) corresponding ground truth of ASI images from (c).

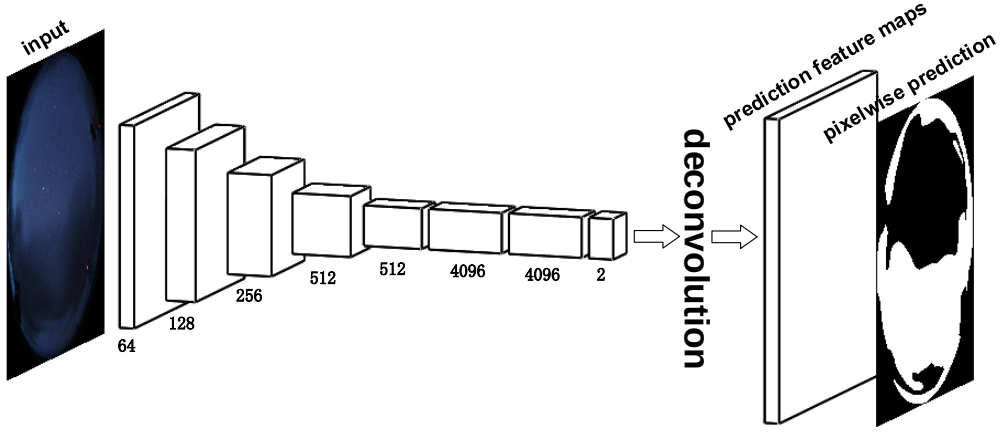

Figure 3. Basic components of FCN model including convolutional layers, pooling layers, activation functions and deconvolutional layers.

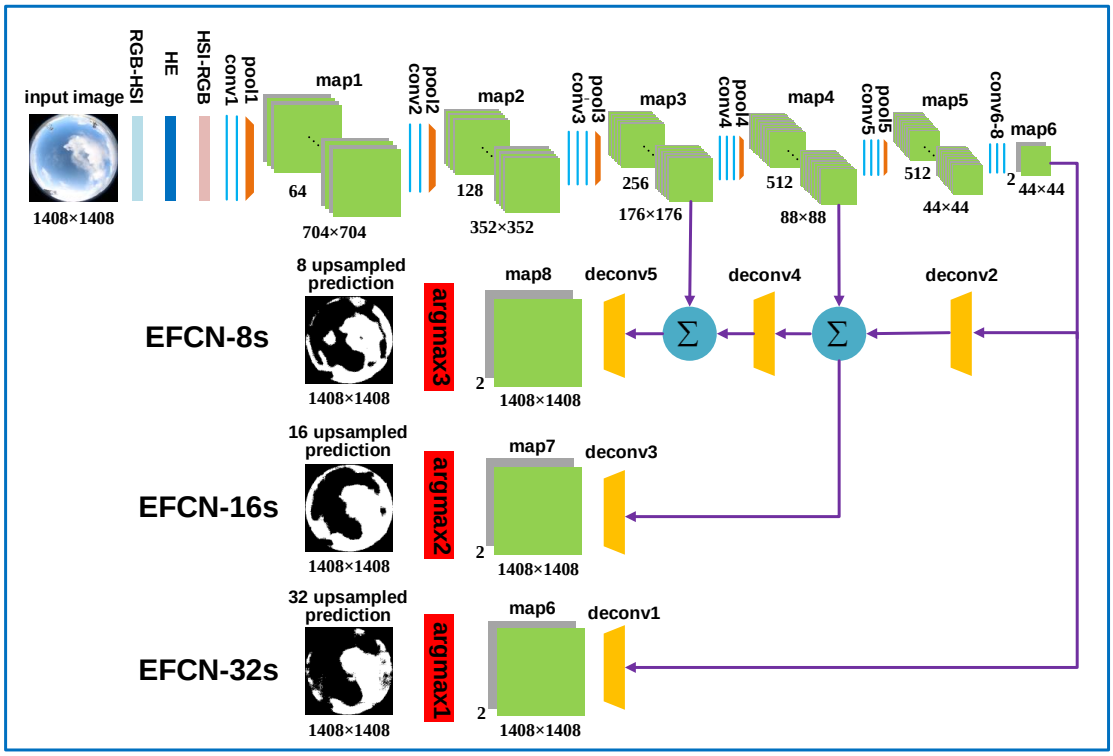

Figure 4. Detailed architecture of EFCN model including RGB-HSI layer, histogram equalization layer, HSI-RGB layer, convolutional layers, pooling layers, deconvolutional layers, skip connection, and activation functions.

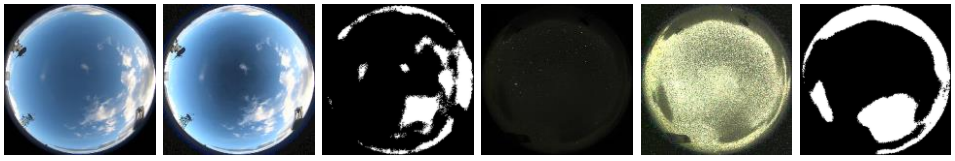

(a) (b) (c) (d) (e) (f)

Figure 5. Framework of the complete proposed automatic cloud segmentation based on EFCN-8s. (a) original diurnal ASI image from test set which is the input test image of the EFCN-8s, (b) enhanced diurnal ASI image using the histogram equalization, (c) diurnal cloud segmentation result using the trained EFCN-8s, (d) original nocturnal ASI image from test set which is the input test image of the EFCN-8s, (e) enhanced nocturnal ASI image using the histogram equalization, (f) nocturnal cloud segmentation result using the trained EFCN-8s.

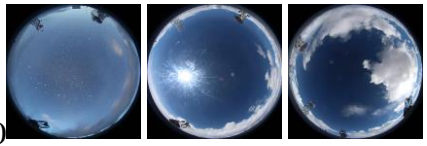

(a)

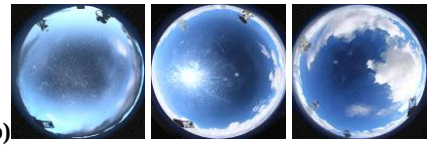

(b)

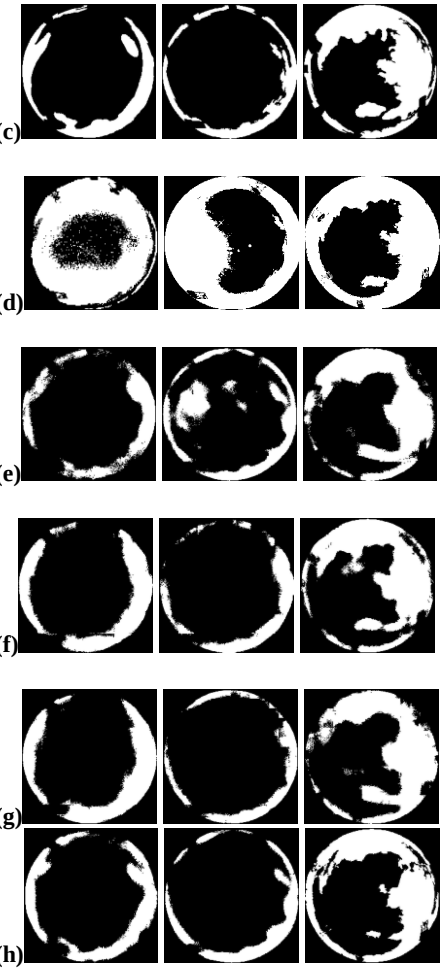

Figure 6. Results of different cloud segmentation algorithms. (a) original diurnal ASI images, (b) enhanced diurnal ASI images, (c) ground truth of the corresponding ASI images in (a), (d) results of OTSU, (e) results of EFCN-32s, (f) results of EFCN-16s, (g) results of FCN-8s, (h) results of the proposed EFCN-8s.

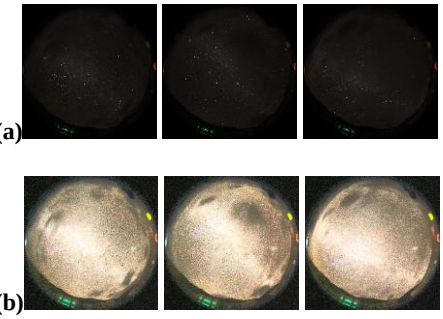

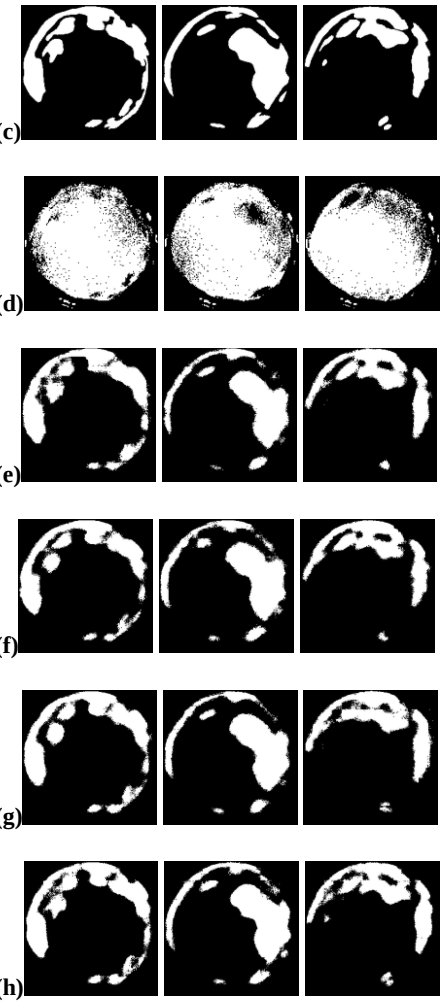

Figure 7. Results of different cloud segmentation algorithms. (a) original nocturnal ASI images, (b) enhanced nocturnal ASI images, (c) ground truth of the corresponding ASI images in (a), (d) results of OTSU, (e) results of EFCN-32s, (f) results of EFCN-16s, (g) results of FCN-8s, (h) results of the proposed EFCN-8s.

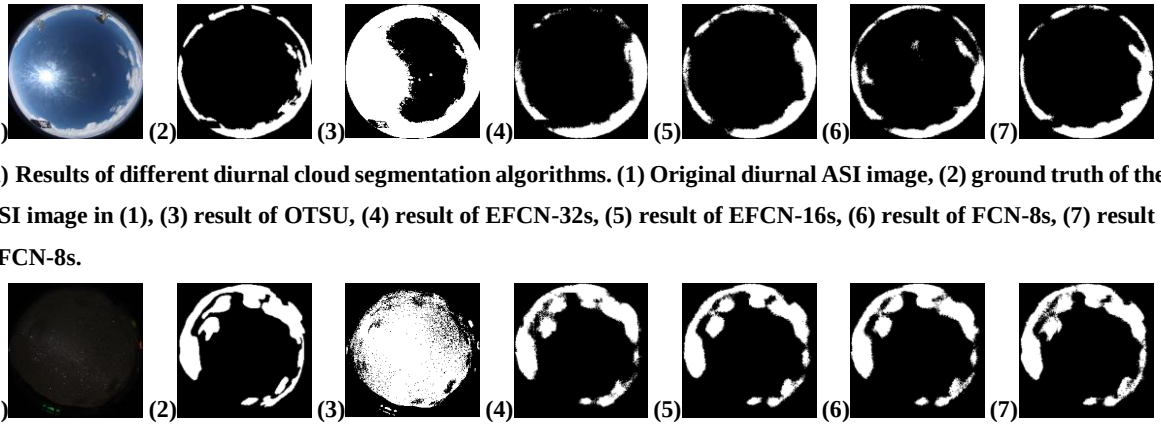

(a) Results of different diurnal cloud segmentation algorithms. (1) Original diurnal ASI image, (2) ground truth of the corresponding ASI image in (1), (3) result of OTSU, (4) result of EFCN-32s, (5) result of EFCN-16s, (6) result of FCN-8s, (7) result of the proposed EFCN-8s.

(b) Results of different nocturnal cloud segmentation algorithms. (1) Original nocturnal ASI image, (2) ground truth of the corresponding ASI image in (1), (3) result of OTSU, (4) result of EFCN-32s, (5) result of EFCN-16s, (6) result of FCN-8s, (7) result of the proposed EFCN-8s.

Figure 8. Results of different diurnal and nocturnal cloud segmentation algorithms.

Table 1 Detailed parameters of the proposed EFCN-8s for segmenting cloud pixels from ASI images.

name	kernel	stride	pad	output size
input image	-	-	-	1408×1408×3
RGB-HSI	-	-	-	1408×1408×3
HE	-	-	-	1408×1408×3
HSI-RGB	-	-	-	1408×1408×3
conv1-1	3×3	1	Yes	1408×1408×64
conv1-2	3×3	1	Yes	1408×1408×64
pool1	2×2	2	No	704×704×64
conv2-1	3×3	1	Yes	704×704×128
conv2-2	3×3	1	Yes	704×704×128
pool2	2×2	2	No	352×352×128
conv3-1	3×3	1	Yes	352×352×256
conv3-2	3×3	1	Yes	352×352×256
conv3-3	3×3	1	Yes	352×352×256
pool3	2×2	2	No	176×176×256
conv4-1	3×3	1	Yes	176×176×512
conv4-2	3×3	1	Yes	176×176×512
conv4-3	3×3	1	Yes	176×176×512
pool4	2×2	2	No	88×88×512
conv5-1	3×3	1	Yes	88×88×512
conv5-2	3×3	1	Yes	88×88×512
conv5-3	3×3	1	Yes	88×88×512
pool5	2×2	2	No	44×44×512
conv6	3×3	1	Yes	44×44×4096
conv7	3×3	1	Yes	44×44×4096
conv8	3×3	1	Yes	44×44×2
deconv1	3×3	32	Yes	1408×1408×2
deconv2	3×3	2	Yes	704×704×2
deconv3	3×3	16	Yes	1408×1408×2
deconv4	3×3	2	Yes	352×352×2
deconv5	3×3	8	Yes	1408×1408×2
argmax1 (FCN32s)	-	-	No	1408×1408×1
argmax2 (FCN16s)	-	-	No	1408×1408×1
argmax3 (FCN8s)	-	-	No	1408×1408×1

Table 2 Comparison of cloud segmentation results of different algorithms on diurnal ASI images.

algorithms	pixel acc	mean acc	mean IU	fw IU
OTSU	0.7751	0.8041	0.6235	0.3448
FCN-8s	0.9086	0.8914	0.7800	0.4239
EFCN-32s	0.9226	0.8859	0.8048	0.4308
EFCN-16s	0.9229	0.8870	0.8049	0.4309
EFCN-8s	**0.9424**	**0.9120**	**0.8481**	**0.4467**

Table 3 Comparison of cloud segmentation results of different algorithms on nocturnal ASI images.

algorithms	pixel acc	mean acc	mean IU	fw IU
OTSU	0.6290	0.6546	0.4868	0.2585
FCN-8s	0.9379	0.9118	0.8578	0.4430
EFCN-32s	0.9414	0.9243	0.8679	0.4465
EFCN-16s	0.9437	0.9311	0.8773	0.4493
EFCN-8s	**0.9504**	**0.9335**	**0.8849**	**0.4541**

Table 4 Comparison of cloud segmentation results of different algorithms on diurnal and nocturnal ASI images.

algorithms	pixel acc	mean acc	mean IU	fw IU
OTSU	0.7021	0.7294	0.5552	0.3017
FCN-8s	0.9234	0.9017	0.8224	0.4329
EFCN-32s	0.9284	0.9025	0.8365	0.4369
EFCN-16s	0.9308	0.8993	0.8327	0.4373
EFCN-8s	**0.9459**	**0.9251**	**0.8686**	**0.4501**

5